Direct Drive: Simulations and Results from the National Ignition Facility

Introduction

In direct-drive inertial confinement fusion[1] nominally identical laser beams are incident on a capsule containing a layer of frozen deuterium–tritium (DT) within a shell made of an ablator such as plastic (CH). The beams ablate the outer material, driving the cryogenic DT layer inward. The shell accelerates during the laser pulse as a result of the pressure from the laser energy deposited in the corona and then decelerates when an outgoing shock is launched once the pressure in the vapor region is higher than the pressure in the inward-moving shell. The shell kinetic energy is then converted to the internal hot-spot energy during stagnation. Ignition requires that the temperature and areal density of the hot spot should be sufficient to generate heating by the alpha particles produced from the D–T fusion reaction. Several measures of target performance have been presented in the literature.[2,3] The minimum fuel energy required for ignition E_{min} considered here is given by[3]

$$E_{min}(\text{kJ}) = 50.8 \, \alpha_{inn}^{1.88} \left(\frac{V_{imp}}{3 \times 10^7 \, \text{cm/s}} \right)^{-5.89}$$

$$\times \left(\frac{P}{100 \, \text{Mbar}} \right)^{-0.77}, \tag{1}$$

where α_{inn} is the adiabat defined as the ratio of the pressure to the Fermi-degenerate pressure in the inner surface of the shell, V_{imp} is the implosion (peak) velocity of the shell, and P is the ablation pressure. Direct drive couples ~3 to 5× more laser energy into the imploding shell than x-ray drive, resulting in larger values of V_{imp} for the same laser energy. From Eq. (1), for the same E_{min} and with larger values of V_{imp}, ignition designs with larger values of α_{inn} are possible in direct drive than from x-ray drive. Direct drive, for example, requires convergence ratios of ≳22 (defined as the ratio of initial radius to hot-spot radius at peak neutron production) to be ignition relevant, whereas x-ray drive requires convergence ratios of 30 to 40. Designs with higher adiabats are more robust to shock mistiming, preheat from fast electrons, or radiation. Higher-adiabat direct-drive designs also benefit greatly from reduced Rayleigh–Taylor (RT)[4] growth. The high power of the velocity

term in Eq. (1) $\left(\sim V_{imp}^{-5.89} \right)$ also indicates that robust predictions of ignition require knowledge of the shell's velocity to very high precision; a 5% decrease in velocity increases the minimum energy required for ignition by nearly 35%.

In direct drive, the implosion velocity and the ablation pressure are primarily determined by coupling the laser into the coronal plasma and the conduction of heat to the ablation surface. The equation of state has been shown to influence these quantities, although to a smaller extent.[5] While the dominant mechanism for laser-energy absorption is collisional absorption (or inverse bremsstrahlung), because of cross-beam energy transfer (CBET)[6] modifications in simulation codes are required to explain observables including capsule trajectory, scattered-light spectra and time histories, and bang times in OMEGA experiments.[7]

In CBET, ion-acoustic waves in the plasma mediate the transfer of energy from an incoming (pump) ray to an outgoing (probe) ray, reducing the energy available for deposition by the most hydrodynamically efficient incoming rays. The CBET gain factor scales as[6,7]

$$d\tau_{CBET} = f_{CBET} \zeta_{pol} \left[\frac{e^2}{c^3 m_e} \frac{n_e}{1 - n_e} \frac{\lambda_0 \langle Z \rangle}{\langle Z \rangle T_e + 3 T_i} \right]$$

$$\times P(\eta) I_{pump} ds, \tag{2}$$

where f_{CBET} is an *ad hoc* multiplier used to explore sensitivity to the model; $\zeta_{pol} = 1/4 \left[1 + (\hat{k}_{pump} \cdot \hat{k}_{probe})^2 \right]$ is the polarization factor; e is the electron charge; c is the speed of light; m_e and n_e are the electron mass and electron density, respectively; λ_0 is the laser wavelength; $\langle Z \rangle$ is the average ionization of the material; T_e and T_i are the electron and ion temperatures, respectively; $P(\eta) = \eta v_\alpha / \left[(\eta v_\alpha)^2 + (1 - \eta)^2 \right]$ is the resonance function with $\eta = (\omega_{pump} - \omega_{probe}) - k_\alpha \cdot V_{fluid} / |k_\alpha| c_\alpha$, where ω_{pump} and ω_{probe} are the pump and probe frequencies, and k_α is the wave number of the ion-acoustic wave given by the wave-matching condition with sound speed c_α and the dimensionless ion-wave damping coefficient v_α; and V_{fluid} is the fluid velocity. The

energy gained or lost is given by $E_0\left[e^{d\tau_{CA}}e^{d\tau_{CBET}}-1\right]$, where $d\tau_{CA}$ is the absorption factor caused by collisional absorption. This model was implemented in the spherically symmetric code *LILAC*[8] and the axisymmetric code *DRACO*.[9] This CBET model was compared to 60-beam OMEGA implosions and, at this time, an overall multiplier $f_{CBET} = 1.5$ is required in *DRACO* to reproduce the observed neutron rates and scattered light. The reason for an overall multiplier is unknown. This fixed value of 1.5 is used in all *DRACO* simulations described in this article.

Differences between OMEGA[10] and National Ignition Facility (NIF)[11] implosions motivate the current experiments on the NIF. The simulated coronal temperature in NIF implosions is ~3.2 keV compared to ~2.75 keV in OMEGA implosions. Additionally, the path lengths d*s* for the rays [Eq. (2)] in the NIF corona are significantly longer; the volume in the NIF corona is approximately a factor of 1.5× larger than OMEGA-scale implosions. Therefore, it is expected that the CBET effect will be considerably larger on the NIF scale. As will be shown later, for the ongoing experiments, CBET decreases implosion velocity by ~18% and the ablation pressure by ~57%, significantly increasing E_{min}. Validating such a model and demonstrating mitigation of CBET are important to the larger direct-drive–ignition program.

The electron-heat conduction from the laser-deposition region to the ablation surface sets up the ablation pressure in direct drive. Nonlocal heat conduction[12] has been shown to play an important role in shock timing in cryogenic DT OMEGA experiments and, in combination with CBET, is required to reproduce all observables related to energetics including trajectories, bang times, time-resolved scattered light, and scattered-light spectra. It is expected that nonlocal electron thermal transport should also play an important role in NIF-scale experiments.

Preheat from two-plasmon decay (TPD)[13] is expected to be larger on the NIF scale compared to OMEGA implosions. In TPD, plasma waves accelerate electrons to energies (≥ 30 keV) with sufficiently long mean free paths so that their energy can be deposited in the cold shell, compromising compression or α_{inn}. TPD is a multibeam instability that requires the overlap of several beams to cooperatively overcome the threshold. In OMEGA implosions, the magnitude of the energy in the source of energetic electrons has been shown to scale with the threshold parameter η:[13]

$$\eta = \frac{I_{n_c/4}\left(\times 10^{14}\,\text{W/cm}^2\right)L_{n_c/4}(\mu m)}{233\,T_e(\text{keV})}, \tag{3}$$

where $I_{n_c/4}$, $L_{n_c/4}$, and T_e are the intensity, density scale length, and electron temperature at the quarter-critical surface, respectively. As mentioned earlier, NIF implosions are characterized by higher coronal temperatures; however, the scale length is also larger—350 μm in the current experiments compared to 150 μm in OMEGA implosions. Note that since the target sizes in the ongoing experiments are determined by the phase plates on the NIF, the scale lengths are smaller than those in ignition-relevant designs (~500 to 600 μm). The extrapolation to longer scale lengths suggests that a larger source of hot electrons is expected on the NIF; however, beam polarizations and beam angles also influence the extent of this instability. One significant difference between OMEGA and NIF experiments is that the ongoing NIF implosions are performed in the polar-direct-drive (PDD) geometry.[14] Beams displaced toward the equator to improve symmetry are incident at oblique angles onto the target. More beams are overlapped in the NIF geometry than on OMEGA but with variations in the beam polarizations and incident angles. These differences motivate experiments on the NIF to estimate the TPD source and its effect on the imploding capsule.

This work presents results from implosion experiments on the NIF. While a subset of results presented in this work has appeared previously,[15] a more-complete analysis that includes the validation of the CBET model in OMEGA PDD implosions, comparison of scattered-light spectra, and time histories with updated simulations that include a first-principles equation of state (FPEOS)[5] is presented here. Also included is a discussion on the reasons for possible differences between simulation and experiment.

This article discusses (1) the target design and (2) results from the experiments, organized by the physics topics—energetics and preheat. Simulated scattered-light spectra show similar trends as observed; trajectories from backlit images and the shapes of the imploding core agree very well, although the trajectory from self-emission images lags the simulation in the experiment. These results and sensitivity analyses to possible errors in CBET modeling, the effect of laser imprint, and fast-electron preheat are examined and future work and conclusions are presented.

NIF Target Design
The primary target type considered in this article has an outer radius of ~1100 μm with an ~100-μm-thick, all-plastic (CH) shell filled with 20 atm of deuterium (D$_2$) gas [Fig. 145.1(a)]. The capsule is irradiated with a laser pulse shape whose temporal history includes a flat foot rising to a main pulse at varying laser intensities.[16,17] The shock launched
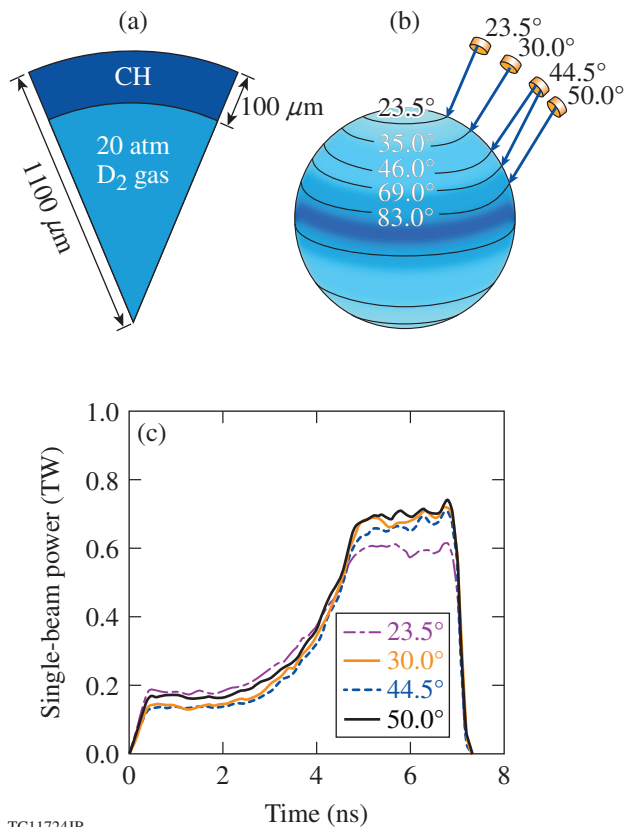
Figure 145.1
(a) Schematic of the target used in a typical polar-direct-drive (PDD) National Ignition Facility (NIF) implosion. (b) The pointing scheme in polar angle used for the PDD implosions. The four original cones at 23.5°, 30.0°, 44.5°, and 50.0° are repointed to the locations shown on the target. (c) Pulse shapes for each of the cones.

insufficient to drive high-performing implosions. Beam profiles used in the x-ray drive ignition campaigns[19] are used in the design. The on-target beam profile is calculated by forward propagating the near-field phase-front information using the code *Waasikwa'*.[20] The laser beams are also defocused by 1 cm to improve symmetry, which is taken into account in the calculation. Since only one set of near-field beam phase-front information is available for each cone, the same calculated profiles are used for all of the beams within a cone.

The beam geometry on the NIF is configured for the axi-symmetric x-ray-drive configuration [Fig. 145.1(b)]. To improve irradiation symmetry, the equator requires additional drive. This is achieved by displacing the beams toward the equator as illustrated in Fig. 145.1(b). The beams on the NIF are arranged in cones at 23.5°, 30°, 44.5°, and 50°. In this PDD geometry, for example, the outer cone located at 50° is displaced to irradiate the target at 83°. The beam configuration in Fig. 145.1(b) is obtained by iteratively adjusting the combination of beam displacements, beam defocus, and beam pulse shapes to reduce shell asymmetry.[16] In addition, beams in cones 44.5° and 50° are displaced azimuthally to improve symmetry. Typical laser pulse shapes for the different cones are shown in Fig. 145.1(c). Notice that the 50° cone is driven with the highest power to provide additional drive in that region. The PDD configuration differs from the spherical-direct-drive (SDD) implosion studies on OMEGA,[16,21] where models have been validated. The lack of drive at the equator is deliberately compensated by displacing beams toward the equa-tor. These beams displaced toward the equator scatter around the target and, consequently, more scattered light appears near the poles in PDD than SDD. SDD is quasi-symmetric; simulations indicate that the scattered light around the target chamber varies by less than 1% rms (root mean square), significantly smaller than PDD. CBET, in particular, is influenced by the PDD beam displacements. More ray crossings occur over a region around the equator; therefore, CBET influences the laser-energy deposition in the region over the equator. As the schematic in Fig. 145.2(a) indicates, an outgoing ray (probe) from the southern hemisphere near the equator acquires energy from an incoming ray (pump) in the northern hemisphere; this excess energy in the outgoing ray can appear as scattered light over the northern polar region. This is also shown in Fig. 145.2(b) in the contour plot of the CBET energy gained per unit volume and normalized to the hydrodynamic time step. The contour plot shows the region where CBET dominates. Most of the energy gain in the rays occurs away from the poles and in a range of polar angles closer to the equator. The projected scattered light around the target chamber is shown in Fig. 145.3 for an OMEGA PDD implosion. The hydrodynamic code *DRACO* with a full three-dimensional

during the foot of the pulse shape sets the implosion at an ignition-relevant adiabat $\alpha_{inn} \sim 3$. The implosions have a low convergence ratio of ~13 (compared to ≳22 for direct-drive igni-tion), defined as the ratio of the initial radius of the fuel–shell interface to the final fuel radius at peak neutron production. The laser energy on target varies from ~350 kJ (for a pulse shape with an intensity of ~4×10^{14} W/cm² at the initial target radius) to ~650 kJ (corresponding to an on-target intensity of ~1.2×10^{15} W/cm²). The pulse shapes are similar although they dif-fer in the duration of the main pulse. The shell is deliberately set at a low implosion velocity of 1.8 to 2.2×10^7 cm/s, com-pared to ignition-relevant values of ≳3.5×10^7 cm/s. The low velocity reduces the instability growth of the most-dangerous modes, which scale linearly with the implosion velocity.[18] This conservative design was chosen because the growth of single-beam nonuniformity (laser imprint) is expected to significantly compromise shell integrity in these implosions (also discussed in **Future Work**, p. 12); the existing laser-beam smoothing is

(3-D) ray trace[22] that includes collisional absorption, nonlocal heat conduction,[23] and FPEOS[5] is used to simulate the PDD implosion. When the effect of CBET is included in the calculation [Fig. 145.3(b)], significantly more scattered light appears near the poles than when only collisional absorption is used to

model the laser-energy deposition [Fig. 145.3(a)]. Scattered-light flux around the target chamber as a function of polar angle, collected using calorimeters in a PDD implosion irradiated with a pulse shape similar to one used in NIF implosions,[24] is shown in Fig. 145.3(c). The locations of the calorimeters are shown as
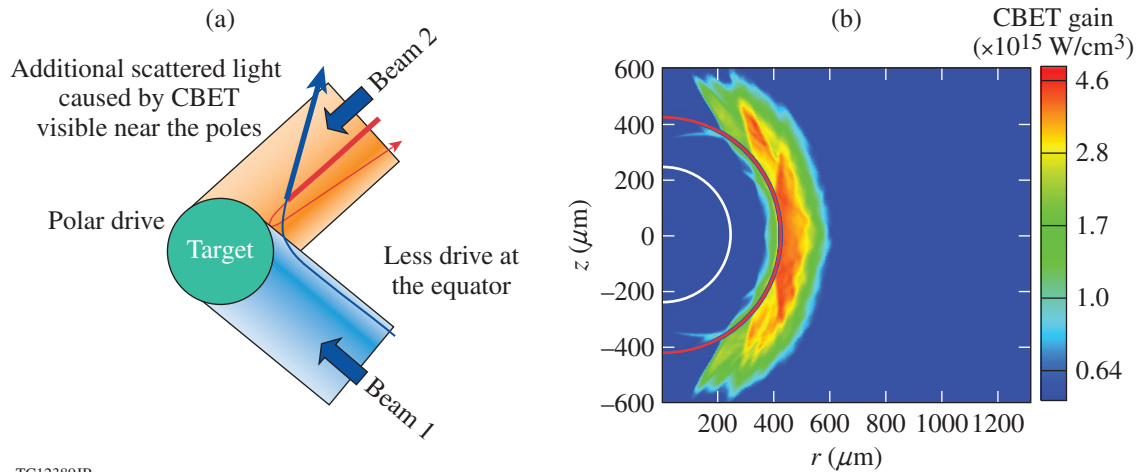
TC12389JR

Figure 145.2
(a) Schematic of cross-beam energy transfer (CBET) in the PDD geometry. The dominant transfer occurs when energy is transferred from an incoming ray to an outgoing ray. (b) Contour plot of energy gained from CBET. The transfer occurs away from the poles; more ray intersections occur away from the poles because of PDD beam displacements.
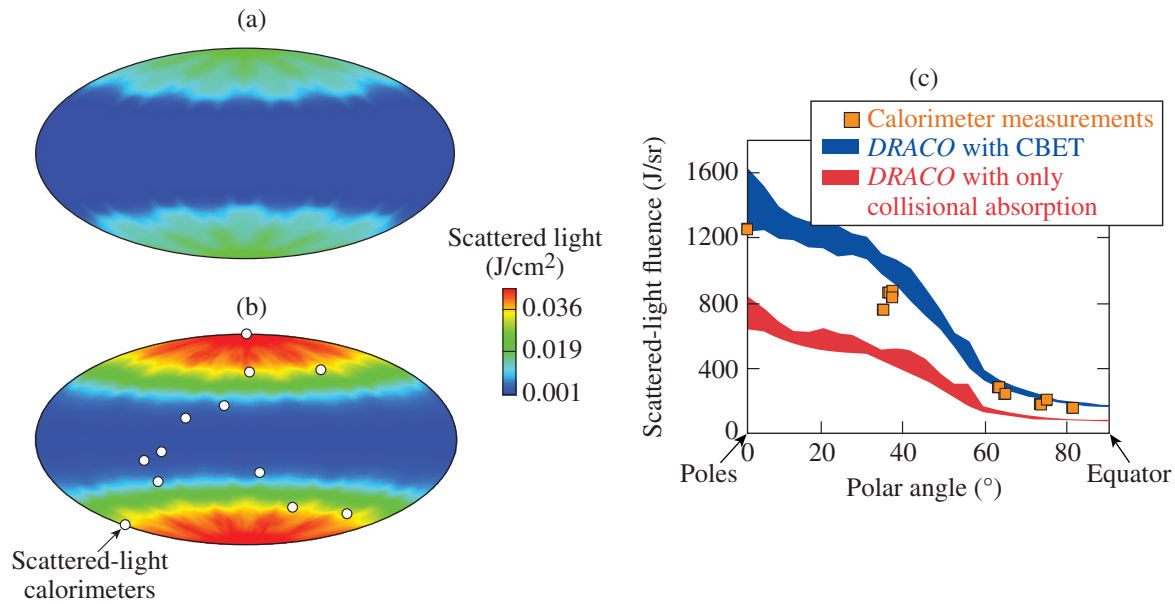

TC12586JR

Figure 145.3
Projected scattered light in the OMEGA target chamber from a simulation that includes (a) only the effect of collisional absorption and (b) the effect of CBET. Circles indicate the locations of the calorimeters in the OMEGA chamber. (c) Scattered-light fluence at the calorimeters in shot 64099 on OMEGA (symbols). The simulation is shown as shaded regions, indicating the minimum and maximum scattered light along the azimuthal angle. Red corresponds to (a)—only the effect of collisional absorption is included. Blue corresponds to (b)—the effect of CBET is also included in the simulation.

circles on Fig. 145.3(b). As the figure indicates, significantly more scattered light appears near the poles when CBET is included in the calculation (blue) compared to when only collisional absorption is included (red). The shaded regions indicate the minimum and maximum light along the azimuth as calculated by the 3-D ray trace. The additional polar light agrees well with observations (symbols), which also show the same trend.

Simulations indicate that the energy transfer from the incoming rays occurs at the center of the beam for rays with the smallest incident angles that are the most hydrodynamically efficient. This results in less drive around the equatorial region; therefore, CBET makes the implosion more oblate than collisional only absorption as seen by the synthetic self-emission images of the imploding shell (Fig. 145.4). Requiring simulations to reproduce the observed shape of the imploding core, i.e., the drive as a function of polar angle, makes PDD a more-stringent test of direct-drive implosion physics than SDD.

(a)   (b)

Collisional absorption only
$t = 6.9$ ns
$R = 526$ mm

CBET model
$t = 7.1$ ns
$R = 531$ mm
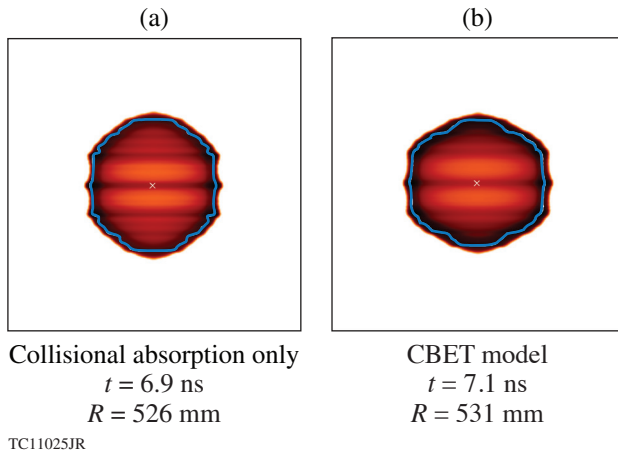
TC11025JR

Figure 145.4
Simulated self-emission images from N150118-002 with (a) only collisional absorption laser deposition included in the calculation and (b) the effect of CBET also included in the calculation.

Results and Discussion

1. Energetics

    a. Results. Energetics on the NIF is inferred from time-resolved scattered light measured using fast diodes[25] and a streak camera.[25] The time-resolved scattered light is plotted in Fig 145.5. The simulation tracks the observations very closely with deviations between 5 and 7 ns. The implication of the excess simulated scattering is unclear. Additional information is also available from the two full-aperture backscatter stations (FABS)[25] that measure the spectrum of scattered light. Figure 145.6(a) shows the spectra observed by the FABS. Features characteristic of implosions are observed in the spectra:

Time-resolved scattered light
N130128-001 (Q31B)
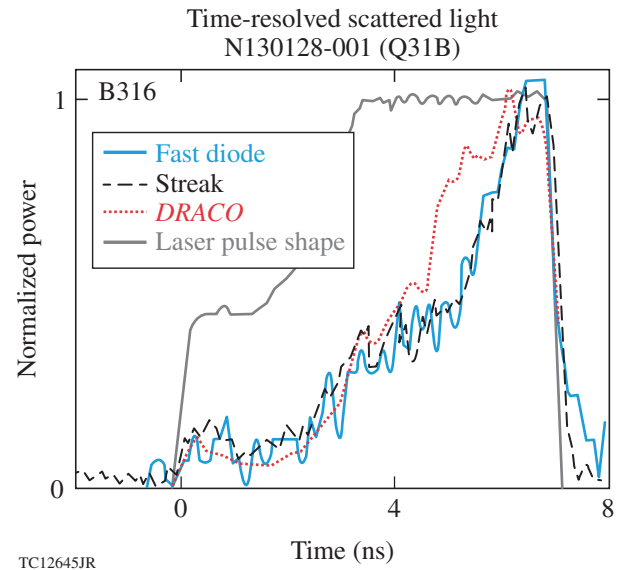
TC12645JR

Figure 145.5
Time-resolved scattered light measured at one location, corresponding to B316, from fast diodes (blue solid line) and optical streak cameras (black dashed and solid lines). Time-resolved scattered light from a simulation including the effect of CBET is also shown (red dotted line).

a rapid blue shift is observed early in time corresponding to corona formation; the red shift at ~2 ns corresponds to the onset of inward motion of the corona during the acceleration phase. Very similar trends are observed in the *DRACO* simulation [Fig. 145.6(b)]. Similar agreement is obtained with the spectra from the other FABS location. Quantitative inferences of the energy in the scattered-light spectrum and the time-resolved light are in progress and are important to further validate the modeling (discussed in the next section).

Trajectories of the converging shell provide information about the laser energy coupled to the target and are measured in two ways: the first uses a gated framing cameras with a 1-mil-thick Be filter (~25 μm) to measure the self-emission of the target,[26] corresponding to photon energies ≳1 keV; the second uses a gated framing camera to measure a radiograph obtained by backlighting an implosion[27] using Fe (~6.7 keV). Excellent agreement is obtained with the CBET model on OMEGA to replicate observed trajectories from self-emission images,[21] while trajectories from backlit images have been explored to a more-limited extent.[27] The design for a backlit implosion requires changes to the beam configuration. Two quads (one from each hemisphere) are removed to irradiate an iron backlighter. The energies of eight neighboring quads and their pointing are adjusted to improve symmetry. Figure 145.7 shows typical images obtained from the framing cameras. The view from the pole records the self-emission. Simulations show that the location of the steepest

gradient corresponds closely to the ablation surface.[26] This location is shown on a typical simulated density profile of the implosion. Notice the circular polar image indicating that the nonuniformity imposed by the removal of quads to irradiate the backlighter has been adequately compensated by the increased energies and repointing of the eight neighboring quads. The view from the equator records the backlit image. The surface of greatest absorption corresponds to the location of the fuel–shell interface, as shown on the same density profile; therefore, the difference in the location of the two surfaces can be interpreted as the thickness of the imploding shell.

Trajectories for different shots are plotted in Fig. 145.8. Simulations are post-processed using the code *Spect3D*[28] to create the self-emission and backlit images. The finite spatial resolution (~20- to 30-μm pinhole size depending on the shot) and gating time window of the cameras (~100 ps) are included in the simulated images. The same analysis is used to extract average radii from the synthetic and measured images.[26,27] The black solid line from the backlit image reproduces the inferred trajectory very well, whereas the red dashed line from self-emission images apparently overestimates the drive. The slopes of the two trajectories indicate that the velocity from the backlit trajectory
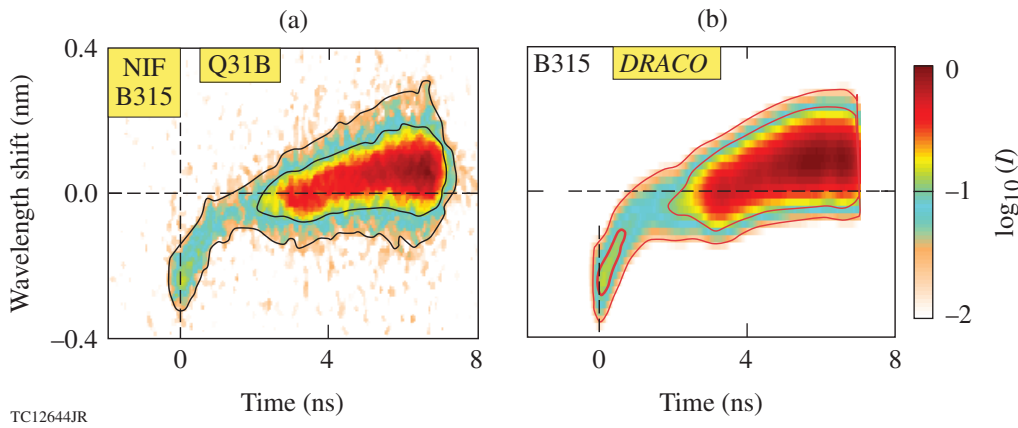

Figure 145.6
Scattered-light spectrum measured using the full-aperture backscatter station (FABS) diagnostic at one location and corresponding to the same location as the diodes. (a) Measured scattered-light spectrum and (b) spectrum from a simulation including the effect of CBET.
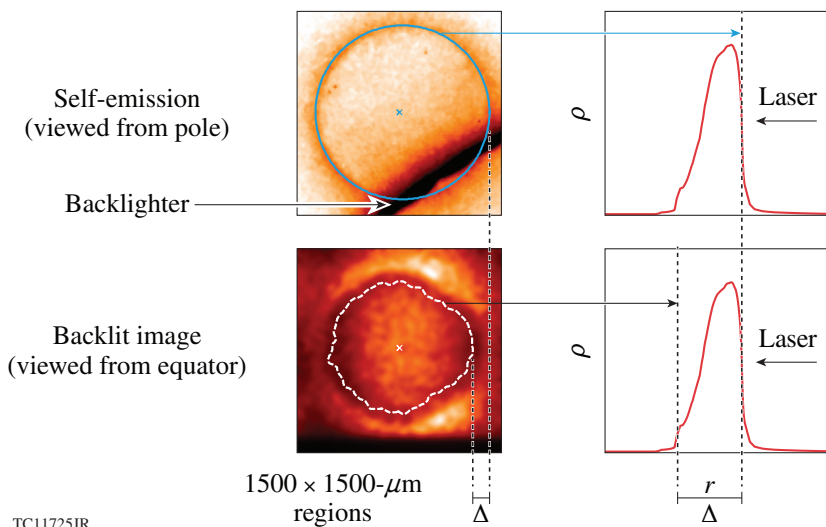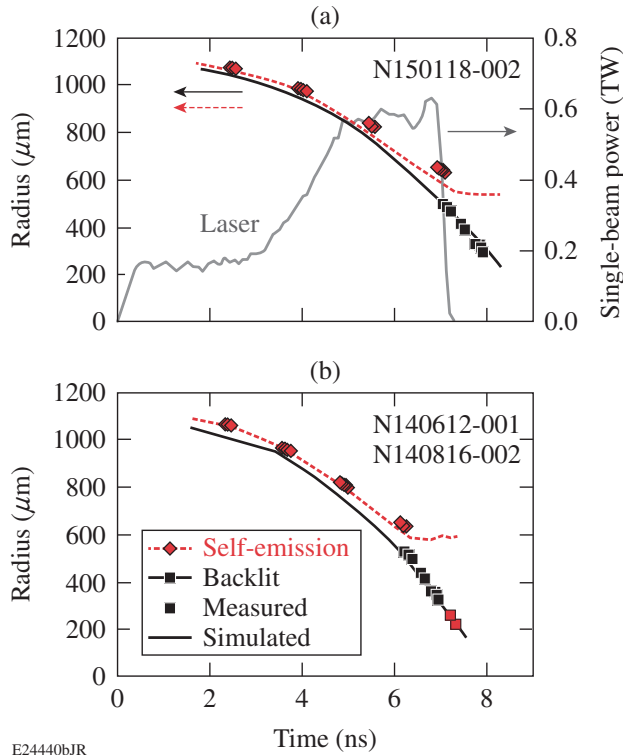

Figure 145.7
Typical self-emission image viewed from the pole and backlit image viewed from the equator (shot N140612-001). Absorption images are obtained at 6.7 keV by backlighting the implosion with Fe. Self-emission images are viewed at ≥1 keV with a Be filter of 1-mil thickness. The lineouts point to the surfaces in the density profile (right) that are extracted from the image.
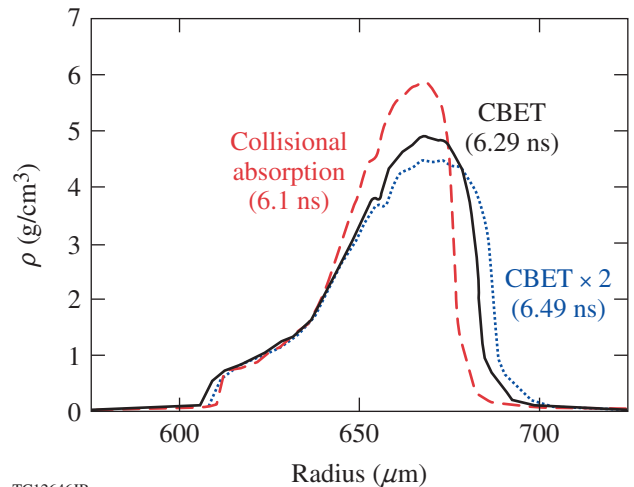
Figure 145.8
(a) Trajectories from backlit images from measurements (black squares) and simulations (black solid line). Trajectories from self-emission images from measurements (diamonds) and simulations (red dashed line) for shot N150118-002. (b) Same as (a) but for shots N140612-001 and N140816-002.

is reproduced to within 1% by the simulation, whereas the trajectory from the self-emission images is overestimated by ~9%. If the self-emission trajectory was representative of the velocity, this would significantly increase $E_{\min}$, compromising ignition. It is, therefore, important to resolve the difference and identify which trajectory, if either, is representative of the true implosion velocity. Note that the inferred shell thickness estimated using the procedure in Fig. 145.7 is larger than the simulated value. The trajectories and shell thickness can be influenced by both 1-D and multidimensonal physics. One-dimensional physics energy includes coupling models and preheat (radiative or fast electron). Multidimensional physics such as Rayleigh–Taylor growth seeded by imprint can also change the location of peak emission or absorption of x rays. It is important to understand if the differences are caused by errors in the 1-D modeling since they influence models used to predict ignition. If imprint was the cause, it is expected to be of less concern since improved beam smoothing[29] and target designs with doped-CH overcoats[30] or Au layers[31] have been shown to mitigate this effect. Each of these factors is discussed below—first qualitatively and then collated in a plot showing the relative magnitude of each of these effects.

b. Sensitivity analysis. Overestimating the predicted velocity of the early shock (resulting from inaccuracies in the modeling of laser coupling or equation of state) can delay the trajectory. If the shock was slower than simulated, the breakout of the shock into the gas would be delayed, postponing the onset of acceleration. Shock mistiming can thicken the converging shell: a higher adiabat results in a lower-density shell that occupies a larger volume during convergence. However, for this pulse shape, the absorption during the low-intensity foot is very high (~95%). The mechanism for absorption during this time is primarily collisional absorption; so any mistiming of the shock is small and its effect on shell thickness and trajectory is insignificant. For example, mistiming the shock during the foot by using a flux-limited diffusive heat-conduction model with flux limiter $f = 0.06$ (Ref. 32) instead of the nonlocal transport delays the shock breakout by less than 20 ps, which only marginally influences trajectory and shell thickness. Therefore, it is hypothesized that the observations cannot be explained by shock mistiming alone.

Sensitivity analysis to the CBET model is examined using the spherically symmetric code *LILAC* by using a multiplier, $f_{\text{CBET}} = 2$, in the gain factor [Eq. (2)]. Figure 145.9 shows the density profiles in the simulation of a NIF-type implosion at different times when the inner surface of the shell has traveled the same distance. The shell becomes increasingly decompressed and the ablation pressure is reduced as the extent of CBET is increased in the modeling (Table 145.I). This also significantly reduces the absorption fraction, suggesting that

Figure 145.9
Density profiles showing the sensitivity of the shell thickness to different extents of CBET (red dashed line: collisional absorption only; black solid line: CBET with $f_{\text{CBET}} = 1$; blue dotted line: CBET × 2 with $f_{\text{CBET}} = 2$).

a detailed quantification of the scattered light is crucial to achieve higher accuracy in the laser-deposition CBET modeling. The implosion velocity, which decreases as the extent of CBET increases in the model, is listed in Table 145.I. This is also shown in Fig. 145.10 through the trajectories of the two surfaces; CBET reduces the velocity of both the surfaces while decompressing the shell. Agreement with the experimentally inferred trajectories requires that the backlit trajectory remains unchanged, whereas the self-emission trajectory becomes apparently slower; therefore, an error in the CBET modeling alone is insufficient to explain the observation.

Preheat from energetic "hot" electrons can also potentially influence the trajectories. The energy in hot electrons is inferred in NIF implosions from the filter-fluorescence x-ray (FFLEX)[33] diagnostic. FFLEX measures the time-resolved x-ray emission in ten channels ranging from ~20 keV to 250 keV. The inferred total cumulative energy E_{hot} is calculated assuming that the entire observed x-ray emission results from the deposition of the fast-electron energy in the CH ablator. A value of $E_{hot} \sim 2.5 \pm 0.3$ kJ

is, therefore, obtained corresponding to ~0.4% of the total laser energy. The hot-electron temperature is inferred by fitting the measured time-integrated x-ray spectrum for the various FFLEX channels. The fit yields a value of 46±3 keV for the shots considered here.[15] This is consistent with temperature measurements on OMEGA.[34] A straight-line deposition formula is used in *LILAC* to simulate the effect of this distribution of electrons on the trajectory and shell thickness.[35] A wide angular divergence of the electrons (240°) is assumed in the model. Studies of TPD in SDD OMEGA implosions using Mo balls of different radii suggest that the electrons are produced at a large divergence angle.[34] Indications of isotropy were also observed in NIF PDD implosions in the DIME[36] (defect-induced mix experiment) campaign.[35] Energetic x rays produced in the DIME NIF PDD implosions are observed via pinhole images and are also isotropic.[37] Therefore, a straight model in the spherically symmetric code *LILAC* is expected to reproduce the sensitivity of the NIF implosion to fast-electron preheat. The observed time-resolved history of the x-ray emission (Fig. 13 in Ref. 15) is calculated by the model—almost no emission is observed until ~4 ns.

Table 145.I: The effect of selected implosion parameters with increasing extents of CBET using the spherically symmetric code *LILAC*. CBET × 2 corresponds to $f_{CBET} = 2$ in Eq. (2). The numbers in parentheses indicate the values (in %) of the quantity relative to the collisional absorption value.

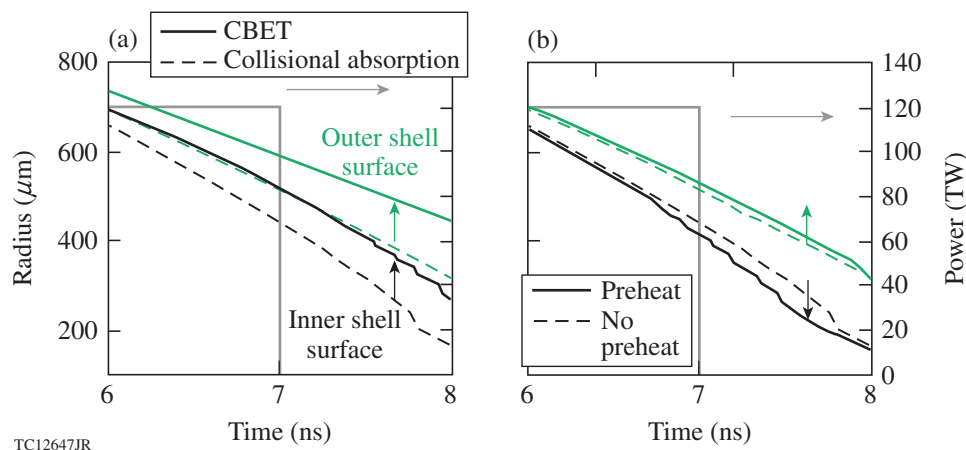| Model	P_{abl} (Mbar)	M_{abl} ($\times 10^6$ cm/s)	V_{imp} ($\times 10^7$ cm/s)	f_{abs}(%)
Collisional absorption	70	1.4	2.2	95
CBET	30 (43%)	0.8 (57%)	1.8 (82%)	75 (79%)
CBET × 2	15 (21%)	0.6 (43%)	1.5 (68%)	64 (67%)

Figure 145.10
Dependence of the backlit and self-emission trajectory to models with (a) collisional absorption only (dashed lines), including the effect of CBET (solid lines) and (b) collisional absorption only (dashed line), including the effect of preheat (solid line). The laser pulse, corresponding to the right axis, is shown for reference.

The emission then increases during the main pulse and stops at approximately the end of the laser pulse. The effect of these electrons on the implosion is shown in Fig. 145.10. A factor of ~2 more electron energy (4.6 kJ) than experimentally inferred is required in the simulation to make the effect more visible on the plot. Preheat increases the shell thickness and decreases the slope of the self-emission trajectory as required to match the observations; however, note that it also increases the slope of the backlit trajectory contrary to what is required to match the observations. The significantly larger magnitude of the preheat source required to observably change trajectories and shell thickness suggests that preheat alone is not likely the cause of the observed discrepancies between simulation and measurements. A comparison of the simulated and inferred self-emission trajectory from a low-intensity shot (~4×10^{14} W/cm² at the initial target radius) also indicates the apparent slowing down of the self-emission trajectory (Fig. 145.11). At this intensity, the energy in fast electrons is estimated to be less than 0.05% of the laser energy at the noise level of the FFLEX instrument—a value that has an insignificant effect on the implosion. This also suggests that fast-electron preheat is less likely a cause for the apparent shell decompression. Fast-electron preheat can be conclusively ruled out only if the backlit trajectory is also well reproduced at the low intensity and the trend in the discrepancy at the two different intensities stays the same. This is being investigated with a low-intensity implosion where a backlit trajectory is also available.
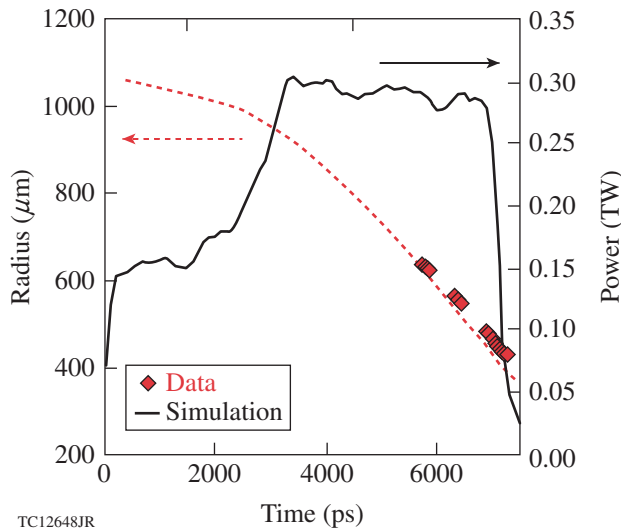
Finally, multidimensional effects are discussed. Single-beam laser nonuniformity imposes perturbations on the target starting at short wavelengths corresponding to ~10 μm ($\ell \sim 600$ at the initial target radius).[9] The effect of laser imprint and the subsequent RT growth is modeled using *DRACO*. Density contours at the end of the acceleration phase for a NIF implosion are shown in Fig. 145.12(a). To make the simulation tractable, only modes up to $\ell \sim 200$ are included in the calculation. The shell is significantly distorted with a relatively intact inner shell. Trajectories from simulated images [Fig. 145.12(b)] indicate that the backlit trajectory is unchanged relative to a simulation with no distortions, whereas the self-emission region moves

(a)

Figure 145.11
Trajectories from a low-intensity implosion (~4×10^{14} W/cm² average on-target intensity at the initial target radius), N130128-001. Only the self-emission trajectory is measured for this shot (red diamonds). The simulated trajectory, including the effect of CBET, is shown as the black solid line.
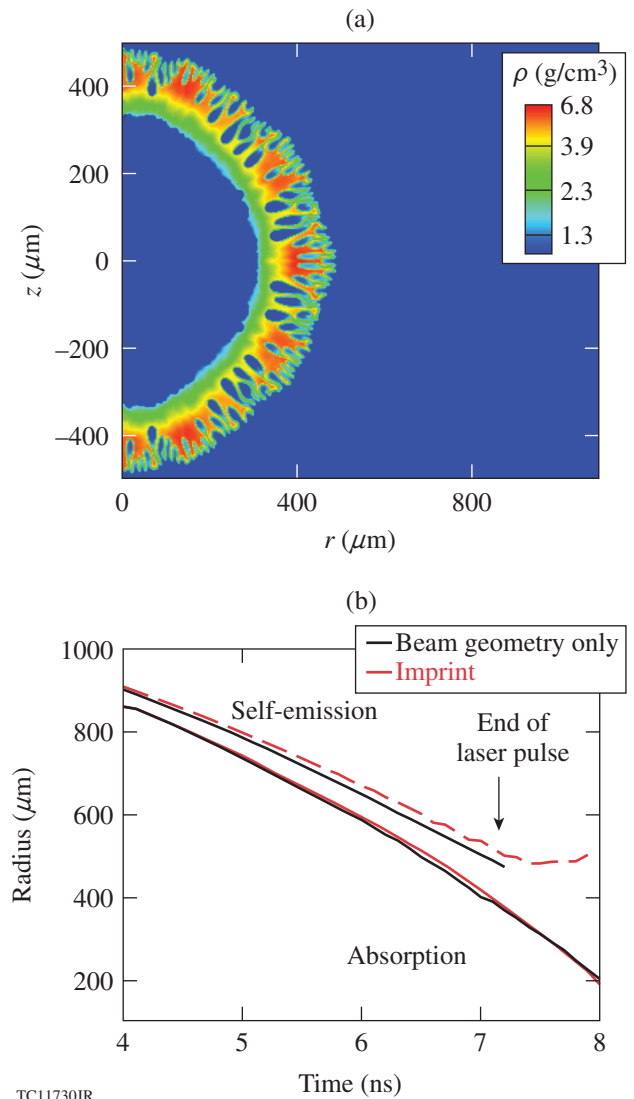
Figure 145.12
The effect of single-beam nonuniformity (laser imprint) is shown as (a) density contours at the end of the acceleration phase and (b) trajectories extracted from post-processed synthetic images of the simulation shown in (a).

farther outward, leading to an apparent decompression of the shell. This trend is consistent with experiments. A larger-scale simulation including modes up to $\ell \leq 600$ is being performed to study the influence of shorter wavelengths on the trajectory and shell thickness. Of the three sources of modeling uncertainty considered so far, only laser imprint shows the correct trends of keeping the backlit trajectory relatively unchanged and causing an apparent slowing down of the self-emission trajectory.

The results from these sensitivity studies are summarized in Fig. 145.13. The percentage increase in shell thickness over the nominal implosion (defined as including CBET, nonlocal transport, and FPEOS) is plotted against the percentage of preheat energy in the fast-electron source. To explore the sensitivity to angular divergence, electrons are launched isotropically and with an angular divergence of 240°. Shell thickness increases slowly with increasing preheat. The observed shell thickness, shown for two shots, is significantly higher than the increase caused by preheat, indicating that preheat alone is insufficient to explain the observed thickness. The increase in thickness from $f_{\text{CBET}} = 2$ is also shown in Fig. 145.13. The relatively small change in shell thickness resulting from any possible error in the CBET model also suggests that energetics are well modeled and is not likely the cause for the observed differences. The increase in shell thickness caused by imprint is shown in Fig. 145.13. Of all the sources considered, imprint

is the dominant contributor to the increase in shell thickness. Imprint also leaves the backlit trajectory unchanged, which is required for consistency with the measurements. It is hypothesized that some combination of the various sources of error and imprint will explain the observations with imprint as the dominant source.

A further indication that the laser drive is well modeled is obtained from the shape of the imploding core. Simulated and observed backlit images are shown in Fig. 145.14 for approximately the same convergence. Note that the shapes are far from round. This is a limitation of the available beam profiles on the NIF. Significantly improved implosions can be obtained with custom beam profiles.[38] The observed shape is very well reproduced by simulations. This is quantified by the radial deviation about the mean radius in Fig. 145.14(c), where the observed and simulated lineouts of the radial deviation are overlaid. Excellent agreement is obtained, suggesting that energetics is well modeled. Small deviations are observed near the pole. This difference is also observed on a lower-

(a) N150118-002 $R = 296 \ \mu$m
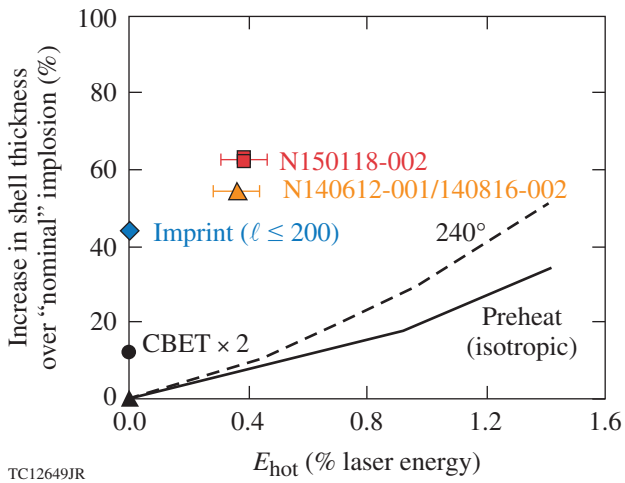(b) 1500 × 1500-μm region $R = 292 \ \mu$m

Figure 145.13
Increase in shell thickness (in %) over the nominal implosion defined as one including the effects of CBET, FPEOS, and nonlocal transport. The symbols with error bars correspond to measured values from framing-camera images. The dashed and solid lines correspond to the simulated effect of preheat. The circle indicates the effect of $f_{\text{CBET}} = 2$ in the CBET model. The diamond indicates the effect of imprint.

TC12649JR

(c) N150118-002
— Backlit observation
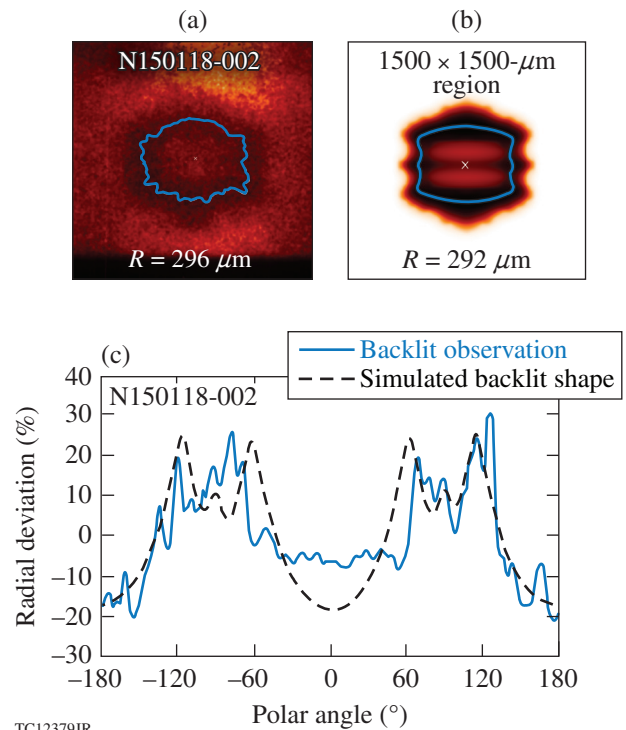--- Simulated backlit shape

TC12379JR

Figure 145.14
(a) Measured backlit image using the Fe line at 6.7 keV. The blue line indicates the surface of maximum absorption. (b) Simulated backlit image. The line shows the surface of maximum absorption. (c) Lineout in polar angle of the radial deviation about the mean at approximately the same convergence for measurements (solid) and simulations (dashed) for shot N150118-002.

intensity shot (Fig. 145.15). The measured and simulated images at the low intensity show reasonable agreement in the shape [Figs. 145.15(a) and 145.15(b)]. The deviation of the lineout about the average radius versus polar angle is shown in Fig. 145.15(c). The gross shape is well reproduced, although the polar region is driven significantly more in the simulation compared to experiment. Since this difference is systematic between two shots, a plausible reason for this difference could be incomplete knowledge of the calculated defocused beam profiles. No measurements of these profiles are available at this time. Moreover, as mentioned earlier, while different beam profiles are calculated for each cone, the same profile is used for all of the beams within the cone. Beam-to-beam variations are not included in the calculation since this information is unavailable.
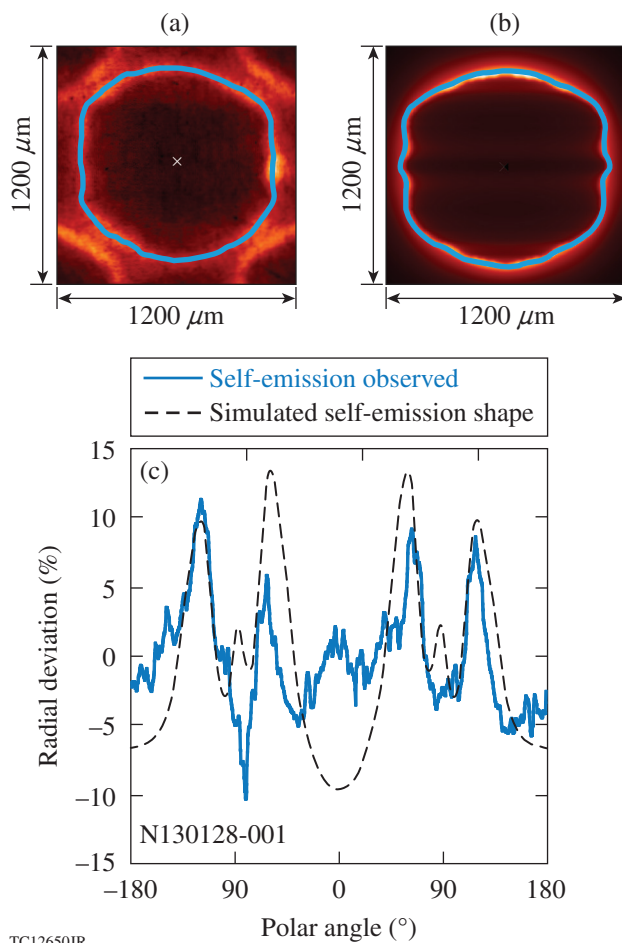

(a) Measured self-emission image. The blue line indicates the surface of steepest gradient of emission. (b) Simulated image. The blue line shows the surface of maximum absorption. (c) Lineout in polar angle of the radial deviation about the mean at approximately the same convergence for measurements (blue solid line) and simulations (black dashed line) for shot N130128-001.

Figure 145.15

c. Preheat. Estimates from FFLEX measurements in NIF implosions indicate that ~0.4% of the laser energy is converted into electron energy at intensities of 8×10^{14} W/cm^2 (the lowest ignition-relevant intensity).[15] Preheat results inferred from FFLEX for shots with varying intensity are summarized in Fig. 145.16. In integrated implosion experiments, typically only the preheat source is inferred from the measurement of bremsstrahlung x rays emitted by the fast electrons. The energy deposited in the cold shell, which is the relevant quantity for designs, is usually calculated using models[35] or estimated from complementary experiments.[39] It has been shown previously from semi-analytic estimates that ignition fails if ≥1.5% of the shell's kinetic energy is deposited as the preheat energy into the shell.[40] A typical ignition design at 1.5 MJ of laser energy, with ~80 kJ of the shell's kinetic energy, can tolerate a maximum of 1.2 kJ or 0.08% of the laser energy deposited in the cold shell without significantly compromising ignition. A similar fraction of ≲1% of the laser energy deposited in the cold shell has been previously obtained from *LILAC* simulations.[41]

The deposited energy in experiments described in this work is estimated using OMEGA implosions. A combination of room-temperature and cryogenic implosions of equivalent mass has been used to infer the energy deposited in the cold shell.[39] This work estimates that ~1/7th of the electron source energy is deposited in the high-density shell. The same ratio is applied to the NIF implosions; the same energy estimated from FFLEX is
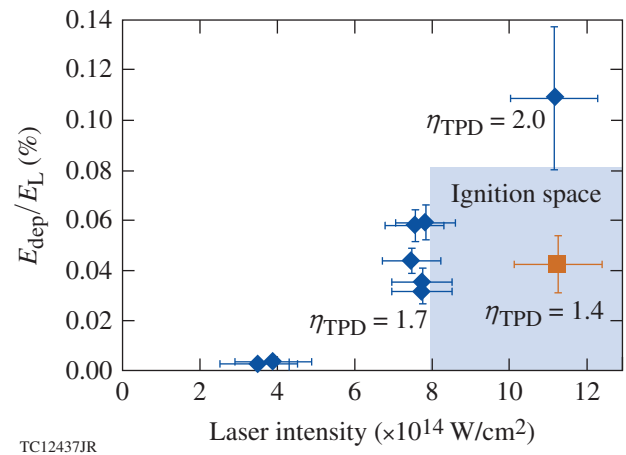
Figure 145.16
Estimated deposited energy from energetic electrons from two-plasmon decay (TPD) as a fraction of the total laser energy versus the polar-angle–averaged, on-target laser intensity during the peak of the laser pulse (measured at the initial target radius) for CH ablators (diamonds) and a target with an outer Si layer (square). The shaded region shows the range of acceptable preheat from fast electrons.

multiplied by this ratio to obtain the hot-electron energy deposited in the shell. Figure 145.16 shows this energy as a fraction of the total laser energy plotted against the on-target intensity (calculated at the initial target radius). The shaded region in the figure shows the acceptable range of intensity and deposited energy based on the analysis presented above. The preheat scales with the calculated values for the threshold parameter, η_{TPD}, consistent with OMEGA implosions. The figure shows that preheat for CH ablators is tolerable at intensities closer to 8×10^{14} W/cm^2, whereas it is clearly at an unacceptable value for ignition at higher intensities. Simulations indicate that with full CBET mitigation, η_{TPD} will increase by nearly 60% to 2.6, possibly resulting in preheat closer to the value at the higher intensity of 1.2×10^{14} W/cm^2. This would result in failure of ignition.

The presence of a mid-Z layer such as Si at the quarter-critical surface during the time of TPD production (the latter part of the main pulse) (Fig. 13 in Ref. 15) has been shown to reduce the preheat source in OMEGA implosions.[42] The reduction in the preheat source is primarily from the higher temperature in the corona because of the high atomic number of Si. A similar NIF experiment with an outer 14 μm of Si overlaid on a CH layer is also shown in Fig. 145.16. In this design, Si is present in the quarter-critical surface throughout the implosion. This clearly reduces the shell preheat to tolerable levels. A similar implosion will be repeated after CBET mitigation to study mitigation of fast-electron preheat.

Future Work

Future work related to NIF experiments will focus on continued model validation. As mentioned earlier, quantification of scattered light is important to disentangle the various effects discussed above and could potentially explain the discrepancy in the self-emission trajectories. Further validation requires larger-scale imprint simulations to isolate the effect of imprint. Measurements of imprint in cone-in-shell geometry[43] will be performed over the next year on the NIF. These experiments will also serve as platforms for future studies of imprint and its mitigation when improved beam smoothing[29] is installed on the NIF. As Table 145.I shows, CBET decreases the mass ablation rate and implosion velocity. Mitigation of CBET is important to recover robust ignition designs. As Eq. (2) shows, detuning the wavelengths of the pump and probe beams will detune the resonance and reduce the volume over which CBET can occur, reducing the magnitude of the effect. This will be studied using the available tunable wavelength capability of the NIF: a maximum of ±2.3 Å in the UV.[44] This value is smaller than what is required to recover more than 50% of the CBET

energy lost in simulations (≳6 Å in the UV).[44] Simulations predict, however, that differences in the shape, trajectory, and the magnitude of scattered light should be observable in the experiment.[44] Other means to improve mass ablation rates such as Be ablators[45] will be explored in the coming year. Finally, TPD mitigation will be studied with a mid-Z layer such as Si after CBET has been mitigated.

The longer-term pre-ignition goal on the NIF is to implode a multilayer target such as the one described in Ref. 21. A mass-equivalent CH layer will replace the cryogenic DT layer in the room-temperature equivalent of the cryogenic target described in Ref. 21. A multilayer target will permit imprint mitigation (through the use of doped ablators such as CHSi or Au layers), the reduction of TPD through the use of a thin Si layer that would be present at the quarter-critical surface only during the latter part of the main pulse (where TPD is evident from fast electrons), and a Be layer to provide an improved mass ablation rate. A high-convergence implosion is not expected from this design since the outer layers of Si radiatively preheat the inner CH layer. This effect is small when a DT layer is used instead of the inner CH layer because of its low opacity. High-convergence direct-drive NIF implosions with CBET and TPD mitigation are possible only in cryogenic DT layered targets.

Ignition attempts require additional investments in hardware on the NIF including improved beam smoothing,[29] custom phase plates,[38] cryogenic target layering, delivery systems, etc. At this time, it is unclear if such an attempt would involve SDD or PDD. A future study will explore the facility and mission impacts of moving some of the NIF beams to enable spherical illumination. The NIF target chamber has ports for such beam placement. The results presented in this work apply to either scheme. Estimating imprint and the effect of laser–plasma interactions at long scale lengths on implosions and their mitigation is a critical component of studying the viability of direct drive as an ignition option.

Conclusions

Results from NIF PDD implosion experiments have been presented. The goal is to test the modeling of energetics and measure the extent of preheat in NIF implosions that have longer coronal density scale lengths than comparable implosions at the Omega Laser Facility. Observables such as the shape of the scattered-light spectrum, time-resolved scattered light, trajectories from backlit images, and the shape of the imploding shell agree very well with simulations. However, the trajectory from self-emission images lags simulations, suggesting a slower trajectory from self-

emission or a thicker shell than simulated. While the cause for this discrepancy is unknown, sensitivity analyses for the various effects that might result in an effectively decompressed shell indicate that errors in energetics modeling, such as those in the CBET model, are likely not the cause. Laser imprint and subsequent Rayleigh–Taylor growth appear to be the dominant source of the observed difference. The CBET model that best reproduces the observations requires the same overall multiplier to the gain factor for both OMEGA and NIF simulations. It is expected that quantifying the scattered light on the NIF will help to identify, if this is indeed the case, and further test model predictability. The fast-electron preheat source in ongoing implosions is at a tolerable level (~0.4% of laser energy at an ignition-relevant intensity of 8×10^{14} W/cm^2 at the initial target radius) corresponding to ~0.06% of the energy deposited in the cold shell. While this is believed to be tolerable for ignition, it is expected that with the mitigation of CBET, the preheat source will increase, leading to more energy deposited in the cold shell. Implosions with mid-*Z* layers have been shown to reduce the preheat source (by nearly a factor of 3). Future pre-ignition plans on the NIF include continued validation of models through measurements of imprint and mitigation of CBET and TPD. All of these mitigation strategies will be studied in an integrated room-temperature implosion involving a target with multiple layers.

ACKNOWLEDGMENT

REFERENCES

1. J. Nuckolls *et al*., Nature **239**, 139 (1972).

2. S. W. Haan *et al*., Phys. Plasmas **18**, 051001 (2011); P. Y. Chang, R. Betti, B. K. Spears, K. S. Anderson, J. Edwards, M. Fatenejad, J. D. Lindl, R. L. McCrory, R. Nora, and D. Shvarts, Phys. Rev. Lett. **104**, 135002 (2010).

3. M. C. Herrmann, M. Tabak, and J. D. Lindl, Nucl. Fusion **41**, 99 (2001).

4. Lord Rayleigh, Proc. London Math Soc. **XIV**, 170 (1883); G. Taylor, Proc. R. Soc. London Ser. A **201**, 192 (1950).

5. S. X. Hu, L. A. Collins, V. N. Goncharov, J. D. Kress, R. L. McCrory, and S. Skupsky, Phys. Rev. E **92**, 043104 (2015).

6. C. J. Randall, J. R. Albritton, and J. J. Thomson, Phys. Fluids **24**, 1474 (1981).

7. I. V. Igumenshchev, W. Seka, D. H. Edgell, D. T. Michel, D. H. Froula, V. N. Goncharov, R. S. Craxton, L. Divol, R. Epstein, R. Follett, J. H. Kelly, T. Z. Kosc, A. V. Maximov, R. L. McCrory, D. D. Meyerhofer, P. Michel, J. F. Myatt, T. C. Sangster, A. Shvydky, S. Skupsky, and C. Stoeckl, Phys. Plasmas **19**, 056314 (2012).

8. J. Delettrez, R. Epstein, M. C. Richardson, P. A. Jaanimagi, and B. L. Henke, Phys. Rev. A **36**, 3926 (1987).

9. P. B. Radha, V. N. Goncharov, T. J. B. Collins, J. A. Delettrez, Y. Elbaz, V. Yu. Glebov, R. L. Keck, D. E. Keller, J. P. Knauer, J. A. Marozas, F. J. Marshall, P. W. McKenty, D. D. Meyerhofer, S. P. Regan, T. C. Sangster, D. Shvarts, S. Skupsky, Y. Srebro, R. P. J. Town, and C. Stoeckl, Phys. Plasmas **12**, 032702 (2005).

10. T. R. Boehly, D. L. Brown, R. S. Craxton, R. L. Keck, J. P. Knauer, J. H. Kelly, T. J. Kessler, S. A. Kumpan, S. J. Loucks, S. A. Letzring, F. J. Marshall, R. L. McCrory, S. F. B. Morse, W. Seka, J. M. Soures, and C. P. Verdon, Opt. Commun. **133**, 495 (1997).

11. J. D. Lindl and E. I. Moses, Phys. Plasmas **18**, 050901 (2011).

12. V. N. Goncharov, O. V. Gotchev, E. Vianello, T. R. Boehly, J. P. Knauer, P. W. McKenty, P. B. Radha, S. P. Regan, T. C. Sangster, S. Skupsky, V. A. Smalyuk, R. Betti, R. L. McCrory, D. D. Meyerhofer, and C. Cherfils-Clérouin, Phys. Plasmas **13**, 012702 (2006).

13. A. Simon, R. W. Short, E. A. Williams, and T. Dewandre, Phys. Fluids **26**, 3107 (1983).

14. S. Skupsky, J. A. Marozas, R. S. Craxton, R. Betti, T. J. B. Collins, J. A. Delettrez, V. N. Goncharov, P. W. McKenty, P. B. Radha, T. R. Boehly, J. P. Knauer, F. J. Marshall, D. R. Harding, J. D. Kilkenny, D. D. Meyerhofer, T. C. Sangster, and R. L. McCrory, Phys. Plasmas **11**, 2763 (2004).

15. M. Hohenberger, P. B. Radha, J. F. Myatt, S. LePape, J. A. Marozas, F. J. Marshall, D. T. Michel, S. P. Regan, W. Seka, A. Shvydky, T. C. Sangster, J. W. Bates, R. Betti, T. R. Boehly, M. J. Bonino, D. T. Casey, T. J. B. Collins, R. S. Craxton, J. A. Delettrez, D. H. Edgell, R. Epstein, G. Fiksel, P. Fitzsimmons, J. A. Frenje, D. H. Froula, V. N. Goncharov, D. R. Harding, D. H. Kalantar, M. Karasik, T. J. Kessler, J. D. Kilkenny, J. P. Knauer, C. Kurz, M. Lafon, K. N. LaFortune, B. J. MacGowan, A. J. Mackinnon, A. G. MacPhee, R. L. McCrory, P. W. McKenty, J. F. Meeker, D. D. Meyerhofer, S. R. Nagel, A. Nikroo, S. Obenschain, R. D. Petrasso, J. E. Ralph, H. G. Rinderknecht, M. J. Rosenberg, A. J. Schmitt, R. J. Wallace, J. Weaver, C. Widmayer, S. Skupsky, A. A. Solodov, C. Stoeckl, B. Yaakobi, and J. D. Zuegel, Phys. Plasmas **22**, 056308 (2015).

16. P. B. Radha, J. A. Marozas, F. J. Marshall, A. Shvydky, T. J. B. Collins, V. N. Goncharov, R. L. McCrory, P. W. McKenty, D. D. Meyerhofer, T. C. Sangster, and S. Skupsky, Phys. Plasmas **19**, 082704 (2012).

17. P. B. Radha, C. Stoeckl, V. N. Goncharov, J. A. Delettrez, D. H. Edgell, J. A. Frenje, I. V. Igumenshchev, J. P. Knauer, J. A. Marozas, R. L. McCrory, D. D. Meyerhofer, R. D. Petrasso, S. P. Regan, T. C. Sangster, W. Seka, and S. Skupsky, Phys. Plasmas **18**, 012705 (2011).

18. C. D. Zhou and R. Betti, Phys. Plasmas **14**, 072703 (2007).

19. L Divol, Lawrence Livermore National Laboratory, private communication (2012); D. A. Callahan *et al*., J. Phys.: Conf. Ser. **112**, 022021 (2008).

20. J. A. Marozas, S. P. Regan, J. H. Kelly, D. D. Meyerhofer, W. Seka, and S. Skupsky, J. Opt. Soc. Am. B **19**, 7 (2002).

21. V. N. Goncharov, T. C. Sangster, R. Betti, T. R. Boehly, M. J. Bonino, T. J. B. Collins, R. S. Craxton, J. A. Delettrez, D. H. Edgell, R. Epstein, R. K. Follet, C. J. Forrest, D. H. Froula, V. Yu. Glebov, D. R. Harding, R. J. Henchen, S. X. Hu, I. V. Igumenshchev, R. Janezic, J. H. Kelly, T. J. Kessler, T. Z. Kosc, S. J. Loucks, J. A. Marozas, F. J. Marshall, A. V. Maximov, R. L. McCrory, P. W. McKenty, D. D. Meyerhofer, D. T. Michel, J. F. Myatt, R. Nora, P. B. Radha, S. P. Regan, W. Seka, W. T. Shmayda, R. W. Short, A. Shvydky, S. Skupsky, C. Stoeckl, B. Yaakobi, J. A. Frenje, M. Gatu-Johnson, R. D. Petrasso, and D. T. Casey, Phys. Plasmas **21**, 056315 (2014).

22. J. A. Marozas, F. J. Marshall, R. S. Craxton, I. V. Igumenshchev, S. Skupsky, M. J. Bonino, T. J. B. Collins, R. Epstein, V. Yu. Glebov, D. Jacobs-Perkins, J. P. Knauer, R. L. McCrory, P. W. McKenty, D. D. Meyerhofer, S. G. Noyes, P. B. Radha, T. C. Sangster, W. Seka, and V. A. Smalyuk, Phys. Plasmas **13**, 056311 (2006).

23. D. Cao, G. Moses, and J. Delettrez, Phys. Plasmas **22**, 082308 (2015).

24. D. H. Edgell, P. B. Radha, V. N. Goncharov, I. V. Igumenshchev, J. A. Marozas, J. F. Myatt, W. Seka, and D. H. Froula, Bull. Am. Phys. Soc. **57**, 343 (2012).

25. D. E. Bower, T. J. McCarville, S. S. Alvarez, L. E. Ault, M. D. Brown, M. P. Chrisp, C. M. Damian, W. J. DeHope, D. H. Froula, S. H. Glenzer, S. E. Grace, K. Gu, F. R. Holdener, C. K. Huffer, J. H. Kamperschroer, T. M. Kelleher, J. R. Kimbrough, R. Kirkwood, D. W. Kurita, A. P. Lee, F. D. Lee, I. T. Lewis, F. J. Lopez, B. J. MacGowan, M. W. Poole, M. A. Rhodes, M. B. Schneider, N. R. Sewall, F. Y. Shimamoto, S. J. Shiromizu, D. Voloshin, A. L. Warrick, C. R. Wendland, and B. K. Young, Rev. Sci. Instrum. **75**, 4177 (2004); J. D. Moody *et al.*, Rev. Sci. Instrum. **81**, 10D921 (2010); P. Datte *et al.*, Proc. SPIE **8850**, 885003 (2013).

26. D. T. Michel, C. Sorce, R. Epstein, N. Whiting, I. V. Igumenshchev, R. Jungquist, and D. H. Froula, Rev. Sci. Instrum. **83**, 10E530 (2012).

27. F. J. Marshall, P. W. McKenty, J. A. Delettrez, R. Epstein, J. P. Knauer, V. A. Smalyuk, J. A. Frenje, C. K. Li, R. D. Petrasso, F. H. Séguin, and R. C. Mancini, Phys. Rev. Lett. **102**, 185004 (2009).

28. J. J. MacFarlane *et al.*, High Energy Density Phys. **3**, 181 (2007).

29. *LLE Review Quarterly Report* **91**, 116, Laboratory for Laser Energetics, University of Rochester, Rochester, NY, LLE Document No. DOE/SF/19460-458, NTIS Order No. PB2006-106662 (2002). Copies may be obtained from the National Technical Information Service, Springfield, VA 22161.

30. G. Fiksel, S. X. Hu, V. N. Goncharov, D. D. Meyerhofer, T. C. Sangster, V. A. Smalyuk, B. Yaakobi, M. J. Bonino, and R. Jungquist, Phys. Plasmas **19**, 062704 (2012).

31. A. N. Mostovych, D. G. Colombant, M. Karasik, J. P. Knauer, A. J. Schmitt, and J. L. Weaver, Phys. Rev. Lett. **100**, 075002 (2008).

32. R. C. Malone, R. L. McCrory, and R. L. Morse, Phys. Rev. Lett. **34**, 721 (1975); J. Delettrez, Can. J. Phys. **64**, 932 (1986).

33. M. Hohenberger, F. Albert, N. E. Palmer, J. J. Lee, T. Döppner, L. Divol, E. L. Dewald, B. Bachmann, A. G. MacPhee, G. LaCaille, D. K. Bradley, and C. Stoeckl, Rev. Sci. Instrum. **85**, 11D501 (2014).

34. B. Yaakobi, A. A. Solodov, J. F. Myatt, J. A. Delettrez, C. Stoeckl, and D. H. Froula, Phys. Plasmas **20**, 092706 (2013).

35. J. A. Delettrez, T. J. B. Collins, and C. Ye, Bull. Am. Phys. Soc. **59**, 150 (2014).

36. T. J. Murphy, N. S. Krasheninnikova, G. A. Kyrala, P. A. Bradley, J. A. Baumgaertel, J. A. Cobble, P. Hakel, S. C. Hsu, J. L. Kline, D. S. Montgomery, K. A. D. Obrey, R. C. Shah, I. L. Tregillis, M. J. Schmitt, R. J. Kanzleiter, S. H. Batha, R. J. Wallace, S. D. Bhandarkar, P. Fitzsimmons, M. L. Hoppe, A. Nikroo, M. Hohenberger, P. W. McKenty, H. G. Rinderknecht, M. J. Rosenberg, and R. D. Petrasso, Phys. Plasmas **22**, 092707 (2015); N. S. Krasheninnikova *et al.*, Phys. Plasmas **21**, 042703 (2014).

37. T. J. Murphy, Los Alamos National Laboratory, private communication (2015).

38. F. Weilacher, P. B. Radha, T. J. B. Collins, and J. A. Marozas, Phys. Plasmas **22**, 032701 (2015); D. Cao, J. A. Marozas, T. J. B. Collins, P. B. Radha, and P. W. McKenty, Bull. Am. Phys. Soc. **60**, 29 (2015).

39. A. R. Christopherson, R. Betti, W. Theobald, and J. Howard, the Ninth International Conference on Inertial Fusion Sciences and Applications (IFSA 2015), Seattle, WA, 20–25 September 2015 (Paper Th.O.2.2).

40. *LLE Review Quarterly Report* **130**, 72, Laboratory for Laser Energetics, University of Rochester, Rochester, NY, LLE Document No. DOE/NA/28302-1058 (2012).

41. *LLE Review Quarterly Report* **79**, 121, Laboratory for Laser Energetics, University of Rochester, Rochester, NY, LLE Document No. DOE/SF/19460-317, NTIS Order No. DE2002762802 (1999). Copies may be obtained from the National Technical Information Service, Springfield, VA 22161.

42. W. Seka, D. H. Edgell, J. F. Myatt, A. V. Maximov, R. W. Short, V. N. Goncharov, and H. A. Baldis, Phys. Plasmas **16**, 052701 (2009).

43. M. Hohenberger, A. Shvydky, P. B. Radha, M. J. Rosenberg, V. N. Goncharov, F. J. Marshall, J. P. Knauer, S. P. Regan, T. C. Sangster, A. Nikroo, and R. J. Wallace, Bull. Am. Phys. Soc. **60**, 164 (2015); A. Shvydky, M. Hohenberger, P. B. Radha, M. J. Rosenberg, R. S. Craxton, V. N. Goncharov, J. A. Marozas, F. J. Marshall, P. W. McKenty, S. P. Regan, and T. C. Sangster, Bull. Am. Phys. Soc. **60**, 118 (2015).

44. J. A. Marozas, T. J. B. Collins, J. D. Zuegel, P. B. Radha, F. J. Marshall, and W. Seka, presented at the 44th Annual Anomalous Absorption Conference, Estes Park, CO, 8–13 June 2014.

45. D. T. Michel, V. N. Goncharov, I. V. Igumenshchev, R. Epstein, and D. H. Froula, Phys. Rev. Lett. **111**, 245005 (2013).